# UC Santa Barbara
## UC Santa Barbara Previously Published Works


### Title
One-Dimensional Edge Contacts to Two-Dimensional Transition-Metal Dichalcogenides: Uncovering the Role of Schottky-Barrier Anisotropy in Charge Transport across MoS2/Metal Interfaces


### Permalink
https://escholarship.org/uc/item/1634v519



### Journal
Physical Review Applied, 15(6)

### ISSN
2331-7043



### Authors
Parto, Kamyar
Pal, Arnab
Chavan, Tanmay
et al.



### Publication Date
2021-06-01

### DOI
10.1103/physrevapplied.15.064068

Peer reviewed



eScholarship.org Powered by the California Digital Library
University of California

# One-Dimensional Edge Contacts to Two-Dimensional Transition-Metal Dichalcogenides: Uncovering the Role of Schottky-Barrier Anisotropy in Charge Transport across $MoS_2$/Metal Interfaces

Kamyar Parto, Arnab Pal, Tanmay Chavan, Kunjesh Agashiwala, Chao-Hui Yeh, Wei Cao, and Kaustav Banerjee*

*Department of Electrical and Computer Engineering, University of California, Santa Barbara, California, USA*

(Received 6 December 2020; revised 15 April 2021; accepted 16 April 2021; published 28 June 2021)

*This paper is a contribution to the joint Physical Review Applied and Physical Review Materials collection titled* Two-Dimensional Materials and Devices.

One-dimensional (1D) edge contacts to two-dimensional (2D) transition-metal dichalcogenides (TMDs), which offer unique features in the design of electronic devices, have recently gained attention. However, the physics of the Schottky barrier of the edge contacts and how exactly it differs from conventional top contacts is not well known. This paper presents a comprehensive *ab initio* density-functional-theory nonequilibrium green's function study of the electrical properties of edge contacts to 2D $MoS_2$. It is observed that, due to the intrinsic terminated edge states, 1D edge contacts to $MoS_2$ are pinned more strongly to a charge-neutrality level that lies closer to the valence band and yields $p$-type characteristics, which are in contrast to top contacts. This Schottky-barrier anisotropy allows edge contacts in $MoS_2$ to outperform top contacts in $p$-type conduction, despite their atomically thin one-dimensional interfaces. Furthermore, the lower limits of contact resistance achievable by edge contacts to $MoS_2$ are estimated. The role of doping, different edge terminations, and Schottky-barrier inhomogeneity in imperfect edge or hybrid contacts are analyzed to assess and provide design guidelines and conditions under which we can utilize edge contacts for various applications including complimentary field-effect transistor (FET) operation.

DOI: 10.1103/PhysRevApplied.15.064068

## I. INTRODUCTION

Since the successful exfoliation of monolayer two-dimensional (2D) semiconducting transition-metal dichalcogenides [1] (TMDs) in 2005, a tremendous amount of research effort has been dedicated to this class of materials. 2D TMDs offer a plethora of intriguing capabilities and unique physics. Their monolayer (1*L*) forms have suitable direct band gaps; high mobilities, even at atomically thin body thickness; and relatively pristine dangling-bond-free surfaces, which have made them the primary contender to replace silicon in future transistor-technology nodes [2–4], thin-film transistors [5], or potential stacked 3D integrated circuit architectures that promise to sustain Moore's law well beyond the foreseeable transistor-scaling roadmap [6]. The strong spin-orbit coupling, in combination with the unique spin-valley locking phenomena in 2D TMDs, has revitalized the spintronics and valleytronic communities [7–10]. Exciting optoelectronic features, such as tunable band gaps [11], rich exciton physics [12,13], and the ability to host single-photon emitters [14,15], have made 2D TMDs a fascinating research front in the photonics community. Biocompatible label-free 2D TMD transistors with high surface-to-volume ratios have found application in biomedical fields [16], such as the design of highly sensitive 2D biosensors [17]. While 2D TMDs continue to draw the attention of many researchers from a multitude of disciplines to the field, there are still a few fundamental challenges that need to be overcome to make 2D TMDs technologically relevant [18].

One such problem was, and still is, the question of how to make low-resistance electrical contacts to 2D materials. Metal-semiconductor contacts in nature tend to form Schottky barriers (SBs) with rectifying behavior [19]. Although our knowledge of engineering TMD-metal contacts for both charge [20–24] and spin [21,25,26] has undeniably progressed, contact resistance of today's conventional contacts to 2D semiconductors still exceeds that of their CMOS counterparts by at least an order of magnitude [27]. In conventional semiconductor technologies, Schottky contacts are engineered to become ohmic by strong doping of the semiconductor surface [28]. Unfortunately, due to their inherent thinness and fragility, 2D TMDs cannot be doped by standard, industry-friendly, and scalable techniques like ion implantation [23]. Other doping strategies [29] that have been explored so far, like *in situ* substitutional doping, surface functionalization, and

*kaustav@ece.ucsb.edu

 © 2021 American Physical Society

electrostatic doping, are either not suitable for large-scale manufacturing [23] or come with a penalty in device metrics, such as high gate-source capacitances. Since a suitable doping mechanism is yet to be discovered, it becomes imperative to identify other "knobs" through which a Schottky barrier can be reduced. One of these knobs is the contact geometry.

2D materials can generally be contacted in two distinct geometries, namely, top and edge contacts [Figs. 1(a) and 1(b)]. However, given the thinness of 2D flakes, it is readily apparent that even the best-case edge contacts may not be pure edges and can have some metal overlap on top. We call this class of contacts impure edge contacts or hybrid contacts [Fig. 1(c)]. In most conventional top contacts [Fig. 1(a)] to 2D materials, metal atoms interact with the 2D semiconductor through weak van der Waals (vdW) interactions. This weak interaction is usually represented as a "tunneling barrier" [20], which adds additional width to the Schottky barrier and reduces the transmission probability of electrons [inset of Fig. 1(a)]. However, in contrast to top contacts, an edge metal contact [Fig. 1(b)] covalently bonds with the 2D layer, resulting in high orbital overlap without the additional vdW gap [20,30] and is predicted to achieve high transmission rates. These higher transmission rates are sometimes mistakenly construed to lower contact resistances in edge contacts. However, attributing the contact resistance solely to the width of the vdW tunneling barrier is a crude oversimplification. This is evident in the recent demonstrations of $MoS_2$ vdW-transferred contacts [31], which, despite preservation of the vdW tunneling barrier, perform better than intimately deposited top contacts. It must be emphasized that the contact resistance is not only a function of the tunneling barrier, but arises as an interplay between both the Schottky barrier height and transmission rates across the interface, in which the latter encompasses the effects of the vdW tunneling barrier. However, the problem becomes more complex, since, as it will be discussed later (Sec. III A), the Schottky barrier and tunneling barrier are also interdependent and cannot be tuned independently of each other. In most earlier research efforts on electrical contacts to 2D TMDs, barring a few limited theoretical studies [20,21,32,33], edge contacts were often overlooked, since (1) pure edge contacts are hard to fabricate and (2) the active area of the metal and semiconductor interface in the edge contact is atomically thin compared with top contacts, thereby the current injection through them is deemed to be limited.

However, in recent years, findings [34–37] have increasingly pointed out the importance and possible advantages of edge contacts. First, 2D material applications can range from monolayer to few-layer bodies contingent on the functionality of the device. In few-layer devices, conventional top contacts [Fig. 1(d)] suffer from a high series resistance for vertical injection due to the highly anisotropic nature of 2D-layered TMDs, which increases the cross-plane resistivity as the layer number increases. To overcome this, edge contacts [Fig. 1(e)] can be used to directly contact the buried layers in few-layer devices to improve performance. This method is especially advantageous in optoelectronics, where the 2D material is encapsulated by *h*-BN layers for protection

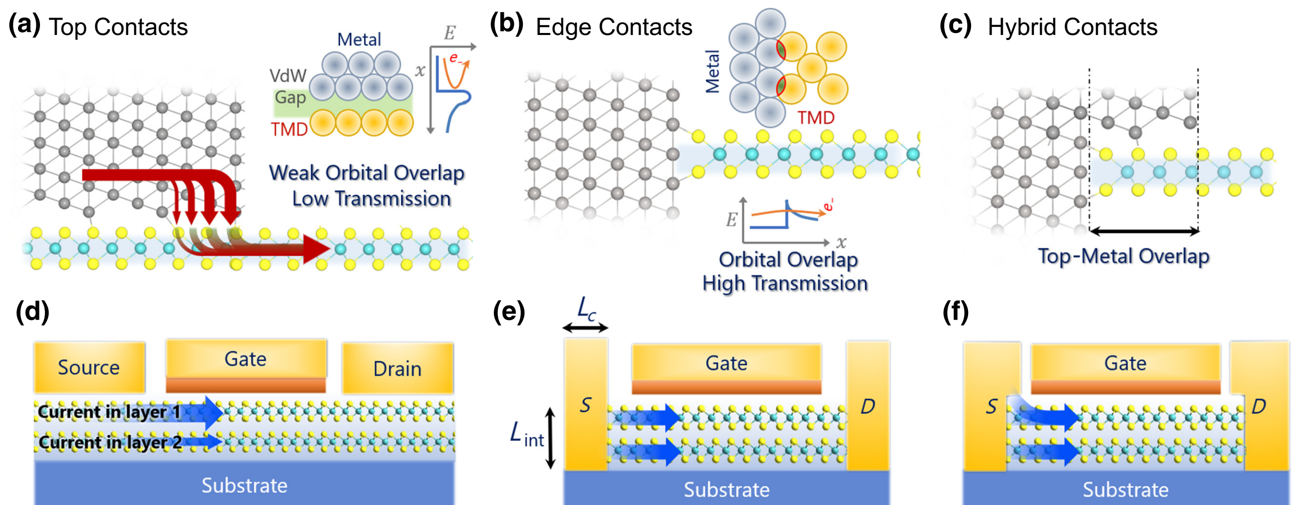


FIG. 1. Possible geometries for metal-$MoS_2$ TMD contacts. (a) Conventional vdW top contacts. Red arrows denote current trajectory, which is predicted to take place, for the most part, along the metal's edge. (b) Edge contacts. (c) Hybrid or impure Edge contacts. (d) Schematic of a bilayer 2D FET with top contact. High anisotropy between in-plane and cross-plane conductivity increases series resistance for the current path in lower layers. (e) Schematic of a pure edge-contacted bilayer 2D FET. Currents in both layers will be relatively equal, since both layers are contacted at once. Also, notably, with a reduction of the contact's physical length ($L_C$), the active interface area ($L_{\text{int}}W$) will stay constant, where $W$ is the device width. (f) Schematic of a bilayer 2D FET with hybrid contacts.

against the ambient and reduced substrate effects. Second, recent studies suggest that current injection from top contacts to monolayer $MoS_2$ happens mostly at the edge of the metal, and conduction to the semiconductor under the metal is prohibited by the electrostatics of the system [35,36] [Fig. 1(a), red line denotes the current path with a transfer length of a few angstroms]. While the study of this effective edge conduction requires more thorough experimental investigations, and the exact ratio of the edge and areal currents depends on the type of metal, semiconductor, nature and strength of metal-TMD atomic overlaps, and their biasing condition, its possibility raises a major conundrum. If electron injection in top contacts happens solely through an atomically narrow active area at the edge of the metal, then what performance advantages do top vdW contacts offer when compared with covalently bonded edge contacts?

Despite these features, the electrical properties of edge contacts remain widely unexplored. Demonstrations of edge contacts [37–44] are still in their infancy, in terms of achieving acceptable contact resistances. Edge contacts to TMDs are typically fabricated in the same manner as that of edge contacts to graphene [45], which is achieved by utilizing *h*-BN encapsulation to isolate the semiconductor surface from the metal contact. An etching process is then utilized to cleave the 2D stack and expose the edge, which is then electrically contacted by a metallization process. Experimentalists have been trying to improve their contact resistances by utilizing ultrahigh vacuum metal deposition and *in situ* argon sputtering techniques to achieve sharper and cleaner junctions [37,42] close to the ideal. However, results still vary by orders of magnitudes (Fig. 2). A clear picture of the physics and electronic dynamics of edge contacts that can reveal their true potential is still missing. Exploration demands a holistic methodology to ascertain the value of different 2D contact approaches and their implications in various 2D device architectures.

Here, taking $MoS_2$ as an example, we utilize density-functional theory (DFT) coupled with the nonequilibrium green's function (NEGF) transport framework to study the electrical properties of lateral, top, and hybrid contacts to 2D $MoS_2$. The manuscript is organized as follows. First, the necessary physics and *ab initio* framework used in the analysis is established in Sec. II. In Sec. III, the edge contacts between $2H$-$MoS_2$ and different 3D metals are studied using this method to investigate the effects of doping, interface geometry, Fermi-level pinning, and edge termination on contact resistance ($R_c$). Moreover, the lower theoretical limits of edge-contact resistances to 2D $MoS_2$ are extracted and compared with conventional top contacts to identify the optimum design space of 2D lateral contacts. This section is concluded by discussing the effects of the Schottky-barrier inhomogeneity on hybrid contacts. Finally, in Sec. IV, we provide an outlook by discussing the implications of the analysis on the design of future 2D devices and examining necessary research directions.

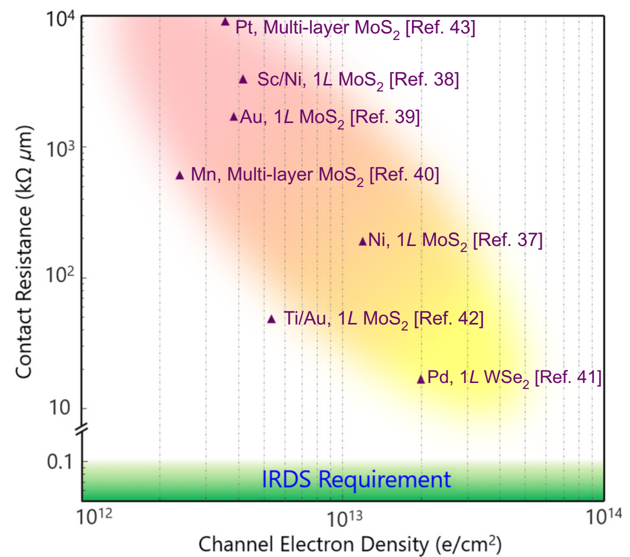


FIG. 2. Edge-contact demonstrations. Demonstrations of edge contacts have improved by over 4 orders of magnitude in recent years due to utilizing stronger gates and maturing of the fabrication techniques. Channel electron densities are extracted by $N = C_{ox}(V_{GS}–V_{th})/q$, where $C_{ox}$ is the oxide capacitance, $V_{GS}$ is the gate-source voltage, and $V_{th}$ is the threshold voltage. As expected, due to the reduction of the Schottky barrier's width at higher carrier concentrations, lower contact resistances can be achieved. Contact resistances, if not reported directly, are approximated by the slope of $I_D$-$V_{DS}$ curves at the highest reported $V_G$ normalized by width of the channel.

## II. METHODS

### A. Physics of Schottky barriers

The most important factor that governs the electrical property of any metal-semiconductor interface is the Schottky barrier. The Schottky barrier for an electron (hole) is defined as the minimum energy from the Fermi level required by electrons (holes) in the metal contact to overcome the energy barrier at the metal-semiconductor interface to reach the conduction (valence) band of the semiconductor [Fig. 3(a)]. Schottky barriers play a significant role in the design of 2D FETs. Electrical characteristics of 2D FETs at short channel lengths are dominated by their contacts and are usually modeled as two back-to-back metal-semiconductor Schottky diodes (known as the 2D Schottky-barrier FET model). Given the importance of Schottky barriers, unfortunately, accurate modeling of Schottky barriers is still a challenging task. Formation of the Schottky barrier is not only dependent on the bulk electronic properties of the materials, but also heavily relies on the detailed physics and chemistry of the interface, which usually becomes an untraceable problem due to the uncertainties and complexities involved.

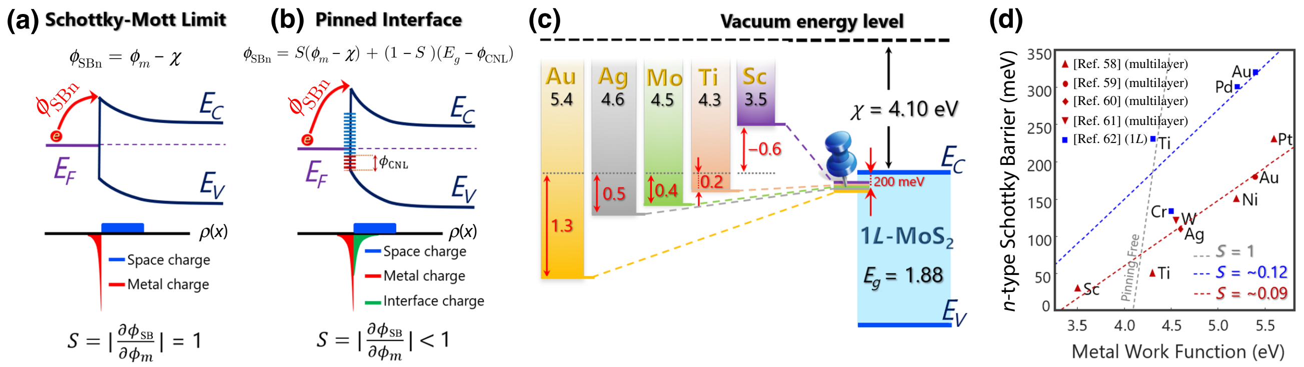


FIG. 3. Fermi-level pinning in Schottky contacts. (a) Band diagram of a hypothetical metal-semiconductor contact in the Schottky-Mott limit. $n$-Type Schottky barrier is determined by the difference of metal's work function ($\phi_m$) and semiconductor's electron affinity ($\chi$). Bottom diagram shows charge distribution across the junction. (b) In a realistic scenario, where mid-gap interface states are present, charging of interface states can dominate the position of the Fermi level at the surface (see SI.1 within the Supplemental Material [48]). In this diagram, it is assumed that the Fermi level lies above the charge-neutrality level (CNL), as is the case for the majority of conventional metals to $MoS_2$. In the presence of interface states, sensitivity of the Schottky barrier to the metal's work function is decreased. (c) Band alignment of several conventional top metal contacts with monolayer $MoS_2$. Difference between metal work function and $MoS_2$ electron affinity is indicated by red arrows. These are the predicted Schottky barriers through the Schottky-Mott rule. However, in experiments, due to Fermi-level pinning, metal Fermi levels are instead pinned to a position approximately 200 meV below $E_c$ (follow dashed lines). (d) Schottky barrier height vs work function for both monolayer and multilayer $MoS_2$. Fermi-level pinning results in decreased $|\partial\phi_{SB}/\phi_m|$ and is centered around the CNL. Notably, Schottky barriers of monolayer contacts are, on average, higher, which can be attributed to the larger band gap of TMDs at the monolayer limit.

Fortunately, many systematic trends still hold true, which provide insight into the physics of Schottky barriers. One such trend and the cornerstone of any Schottky-barrier model is the Schottky-Mott rule. The rule predicts that the $n$-type Schottky barrier ($\phi_{SBn}$) must follow the $\phi_{SBn} = \phi_m - \chi$ relation, i.e., the electron Schottky barrier is precisely proportional to the difference of the metal's work function ($\phi_m$) and semiconductor's electron affinity ($\chi$) [Fig. 3(a)]. This prediction deviates from experimental results, which reveal that, for conventional semiconductors, such as Si and GaAs, the barrier height weakly depends on the metal's work function and is usually fixed at a value about 1/3 of the band gap (referenced to valence-band maxima), irrespective of the metal used [46]. The primary reason why the Schottky-Mott rule deviates from experimental trends lies in the interface or, more specifically, the absence of any interface physics in the Schottky-Mott rule. When a metal comes into contact with the semiconductor, the atomic arrangement of atoms at the interface is altered, chemical bonds are formed, and charge is redistributed into newly formed electronic mid-gap states that are a contribution from the orbital mixture in both metal and semiconductor. As a result, the Fermi level at the interface, which determines the Schottky barrier, is now governed by the filling of the interface states, rather than the bulk electronic bands, as predicted by the Schottky-Mott relation [Fig. 3(b)]. In other words, the Fermi level becomes "pinned" [46] to an energy level that minimizes the surface charge, and the Schottky barrier becomes less sensitive to the metal's work function [Figs. 3(a) and 3(b)]. This effect is captured through the definition of the $S$ parameter, which determines the sensitivity of the Schottky barrier to the metal's work function [Fig. 3(b)]. In the absence of interface states, $S = 1$ and the Schottky barrier becomes a function of the metal's work function. In the presence of a high density of interface states, $S$ becomes negligible, and the Schottky barrier is determined by the charge-neutrality level (CNL), irrespective of the work function. The CNL is the energy level at which the surface charge is minimized and is determined by the energy at which mid-gap states transition from donorlike to acceptorlike in nature [47]. In bulk semiconductors, such as Si, the Fermi-level pinning problem is addressed by heavy doping of the contact regions, which makes the SB width vanishingly small or nearly transparent, leading to the realization of ohmic contacts. We dedicate SI.1 within the Supplemental Material [48] to a quantitative semiclassical discussion of Fermi-level pinning, SI.2 within the Supplemental Material [48] is dedicated to an atomistic picture; for a more thorough analysis, readers are referred to the seminal papers by Tung [49,50]

In 2D TMDs, Fermi-level pinning haunts the electrical contacts to an even greater extent [21,23], especially in the absence of reliable doping techniques: the electrical responses of most metal-TMD contacts are governed by their Schottky barriers. Conventional top contacts to 2D TMDs are dominated by a high concentration of defect states ($D_{it}$) at the surface. This mostly stems from the fact that the quality of 2D growth is still far from that of silicon technology. For instance, 2D $MoS_2$ surfaces that

are theoretically supposed to be "pristine" or dangling-bond-free regularly exhibit $D_{it}$ values in the order of $10^{11}$ to $10^{12}$ cm$^{-2}$ contingent on their growth and exfoliation conditions [51]. While the atomic origin of these states is still under debate and has potentially been attributed to both S vacancies [52–55] and transition-metal defects [56], in $MoS_2$, they nevertheless introduce states with energies very close to that of the conduction band. To respond to these defect states, the effective charge-neutrality level moves close to the defect energy levels, and, as a result [57], the Fermi level becomes pinned to these high-density defects and forms *n*-type Schottky barriers with heights in the range of 50–200 meV [58–61] for multilayer and 100–350 meV [62] for monolayer $MoS_2$ [Figs. 3(c) and 3(d)]. Given the importance of Fermi-level pinning, several questions naturally come to mind. First, where does the Fermi level become pinned for lateral (edge) contacts? And how will it be different with respect to the top contacts? The next question we address arises from the atomically thin interface area of lateral 1D interfaces. Does the atomically thin cross section of the one-dimensional interface limit the minimum contact resistance; if so, what are the lower theoretical limits of 1D (edge) contacts?

To analyze the electrical properties of the lateral 1D interface and answer the aforementioned questions, an *ab initio* transport framework is required to provide a quantitative picture of the band alignments, the transmission probability of each available state, and finally the contact resistances for different contact configurations. In this study, we utilize an *ab initio* DFT NEGF transport framework using Synopsis QuantumATK [63,64]. Lateral interfaces of five conventional 3D metals (Sc, Ti, Mo, Ag, Au) with $MoS_2$ are analyzed. The chosen metals cover a broad range of work functions (~3.5 to 5.2 eV), which allow us to probe further into the physics of Schottky-barrier formation at these interfaces. Both *n*-type and *p*-type barrier heights are extracted at various doping levels for different metals. Electron transmission spectra are extracted using the NEGF formalism [65,66] and finally $R_c$ is obtained through the Landauer formalism to estimate the lower limits of contact resistance.

To introduce and justify our analysis method, we first apply it to the $Ag/MoS_2$ interface as an example. One should note that this analysis method is not specific to lateral 2D interfaces and can be used to analyze a variety of interfaces. DFT NEGF calculations are performed using the Perdew-Burke-Ernzerhof (PBE) variant of the generalized gradient approximation (PBE GGA) exchange-correlation functional [67]; Hartwigsen-Goedecker-Hutter (HGH) pseudopotentials; $11 \times 3 \times 11$ and $11 \times 3 \times 415$ Brillouin zone *k*-point sampling for DFT and NEGF calculators, respectively; 240 Rydberg density mesh cutoffs; and a 0.05 eV/Å maximum force constant for geometry optimizations. We further employ Grimme's DFT-D2 dispersion correction [68] to account for vdW interactions. The GGA HGH with DFT-D2 vdW correction setup has been previously identified to reproduce the experimental band structure and band gap of $MoS_2$ (SI.3 within the Supplemental Material [48]) reasonably well and has been widely used in the literature to probe the physics of TMDs. To avoid redundancy, SI.4 within the Supplemental Material [48] is dedicated to the complete simulation results of all other interfaces.

Next, a lateral interface between the Ag ⟨100⟩ plane and $MoS_2$ zigzag (ZZ) Mo truncated interface with sulfur passivation (Mo-ZZ-2S) is constructed, as seen in Fig. 4(a). Given the fact that $MoS_2$'s edge has the lowest formation energy in molybdenum zigzag terminated geometry with sulfur dimers (Mo-ZZ-2S) [69,70], we limit this study to the zigzag truncated interfaces. The metal plane orientation is chosen to allow us to construct supercells with low lattice mismatch and absolute strain (below 3%, with the entire strain applied to the metal to ensure that the semiconductor band gap, and hence, the Schottky barrier, is unaffected) and are small enough to be computationally feasible. Next, the structure is geometrically relaxed, which allows for the formation of chemical bonds and any inevitable structural deformation as a result. Next, a two-electrode device is created for NEGF transport simulations [Fig. 4(b)]. An important requirement for the NEGF framework is that any built-in potential in the scattering region (due to interface effects, defects, etc.) must be sufficiently screened out before reaching the metal and semiconductor electrodes [66,71]. To satisfy this requirement, nine atomic layers of metals, sufficient to screen any interface effects on the metal side [20], are included in the scattering region. Similarly, the length and doping of the semiconductor region must be chosen sensibly to accommodate the depletion width ($L > W = \sqrt{2\varepsilon_s V_{\mathrm{BI}}/qN_d}$, where $\varepsilon_s$ is the semiconductor dielectric constant, $V_{\mathrm{BI}}$ is the built-in potential, $N_d$ is the doping density, and $q$ the elementary charge). To assess the effect of doping on contact resistance, $MoS_2$ is doped by rescaling the valence charge of individual atoms using the atomic compensation charge method at eight different doping concentrations ($\pm 6.85 \times 10^{11}$, $\pm 6.85 \times 10^{12}$, $\pm 6.85 \times 10^{13}$, $\pm 6.85 \times 10^{14}$ cm$^{-2}$) with suitable semiconductor lengths ($L > W$) (300, 300, 100, and 100 Å, respectively). Next, the projected local density of states (PLDOS) of the system at different doping levels is calculated along the transport direction (*x* axis), which gives an overall view of the band alignment of the metal-semiconductor contact. Figure 5(a) shows the PLDOS plots of the $Ag/MoS_2$ (Mo-ZZ-2S) interface at eight different carrier concentrations. Moreover, to better visualize band movements in the depletion region, the macroscopic in-plane average of the Hartree difference potential ($\langle V_H \rangle$) is superimposed on the PLDOS picture. The Hartree potential is the local electrostatic potential of the system governed by Poisson's equation. Far from the interface, the macroscopic average

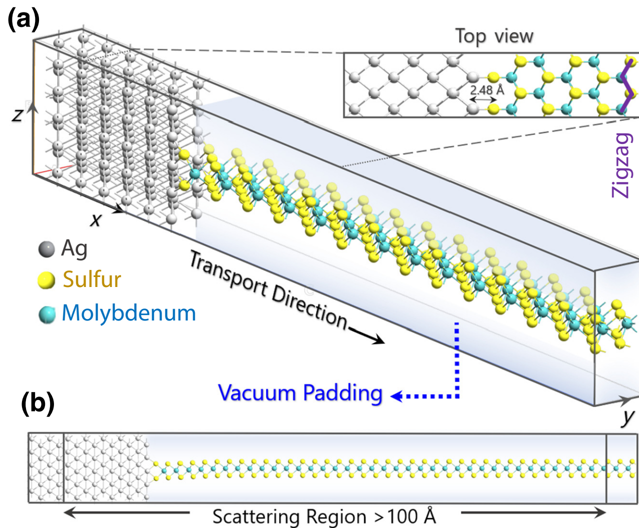


FIG. 4. (a) Supercell geometry for DFT calculations between metal and $MoS_2$ zigzag interface with sulphur dimers ($MoS_2$-ZZ-2S). The addition of about 7 Å of vacuum padding is necessary to eliminate any interlayer coupling effects that QuantumATK may inadvertently induce by repetition of the unit cell in the $z$ direction (b) Two-electrode device used for NEGF simulations. Length of the scattering region is chosen in accordance with doping levels to guarantee screening of the interface potential.

of the Hartree potential follows the semiconductor's band bending due to the depletion charge. Close to the interface, the potential is altered by the interface dipole (see SI.2 within the Supplemental Material [48] for more discussions on atomistic modeling of Schottky-barrier theory for the interface dipole). From Fig. 5(a), i–viii, as predicted, the depletion region starts to shrink with increased doping. Also, it can be generally observed that the lateral Ag-$MoS_2$ contacts show a more dominant $p$-type behavior (smaller $p$-type barriers compared with $n$-type barriers). Another interesting feature of PLDOS plots is the visualization of the metal-induced gap states (MIGs) [72]. At the location of the physical interface [denoted by yellow dashed lines in Fig. 5(a), iv and viii], DOS in the semiconductor gap do not sharply go to zero. In fact, even a few angstroms away from the actual metallurgical interface, MIGs are present in the mid gap and decay into the semiconductor. Figure 5(b) shows the energy distribution of the mid-gap states on the semiconductor side at the Ag/$MoS_2$ interface. The presence of MIGs also means that there is no clear electronic separation between the semiconductor and the metal in the interface region. Therefore, an estimation of the barrier height solely through the PLDOS plots will not be accurate, since one cannot pinpoint a specific location for the electronic interface.

### B. Extraction of metal-2D TMD barrier heights

Two methods can be used to extract the barrier height from the DFT NEGF results. Stradi *et al.* [66] propose that one can extract the barrier height from the energy difference between the maximum of $\langle V_H \rangle$ to the metal's Fermi level [see Fig. 5(a), i]. The position of maximum $\langle V_H \rangle$ indicates the location where the interface dipole begins to affect the potential and serves as a good approximation of the electronic interface position. Unfortunately, this method works only when the polarity of the interface dipole on the semiconductor side has the opposite sign to the depletion charge, which will guarantee the occurrence of an extremum in the Hartree potential. This is the case for $n$-type contacts to $MoS_2$, whereas, as the sign of the depletion charge is flipped in $p$-type contacts, no extrema in $\langle V_H \rangle$ can be observed anymore (see Figure SI.1.3 within SI.1 of the Supplemental Material [48] for more details). Hence, this method cannot be generalized for all contacts.

A more rigorous approach is to extract the barrier heights from the NEGF transport results, which relies on referencing the energy at transmission turn on with the Schottky barrier height. The transmission spectrum denotes the probability of available states at each energy to transmit through the interface. The minimum energy after which the electrons can conduct is the inherent definition of the electronic barrier height. It can be seen from Fig. 5(a), i–viii, that the transmission spectrum is always zero in the band gap, since there are no available states to conduct electrons. At energies slightly higher than $E_{C,\mathrm{NR}}$ (conduction band in the neutral region), when the depletion region is present, there are available states on both the metal and semiconductor sides. However, the barrier at the interface still blocks transmission and $T(E)$ remains negligible. It is only at higher energies where electrons gain enough energy to surpass the interface barrier when $T(E)$ begins to increase. Interestingly, this onset of transmission turn on (defined as the point where the $T(E)$ reaches 1% of the maximum transmission [73]) coincides well with the maximum of $\langle V_H \rangle$, which indicates that the first method is successful at predicting the barrier height.

At this point, we should emphasize that we intentionally do not use the term "Schottky barrier" when referring to barriers seen in Fig. 5(a), i–viii. First, the barrier heights extracted from the onset of the transmission spectra are simply activation energies, which are not necessarily equal to the Schottky barrier. For instance, at high doping levels, due to the thinning of the Schottky barrier's width, the thermally assisted tunneling current (thermionic field emission) can conduct through the barrier [19,74] [Fig. 5(c), ii]. In such cases, the estimated barrier from the transmission spectrum can be smaller than the actual Schottky barrier. Second, it is notable that, despite the common misconceptions that arise by neglecting the space-charge term in Schottky-barrier calculations [19], the Schottky barrier itself is inherently dependent on semiconductor doping and can be substantially lowered [see Fig. 5(c), iii] at doping levels exceeding $10^{20}$ cm$^{-3}$ [19] (see SI.1 within

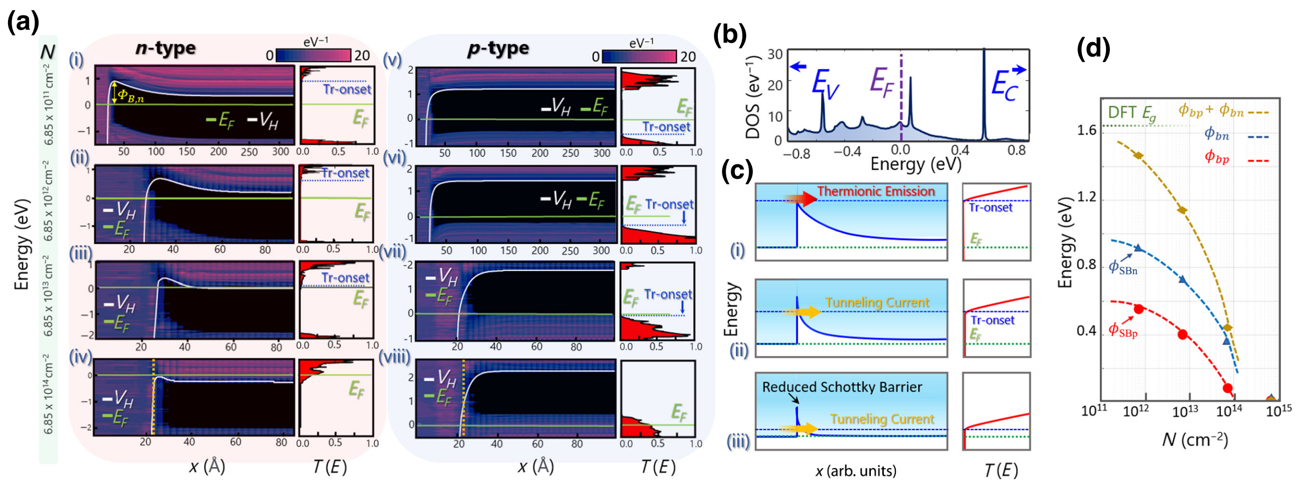

FIG. 5. Schottky-barrier extraction using DFT NEGF for Ag/$MoS_2$ interface. (a) Superimposed PLDOS, Hartree potentials, and transmission spectra at various doping levels: (i) $n$-type $6.85 \times 10^{11}$ cm$^{-2}$, (ii) $n$-type $6.85 \times 10^{12}$ cm$^{-2}$, (iii) $n$-type $6.85 \times 10^{13}$ cm$^{-2}$, (iv) $n$-type $6.85 \times 10^{14}$ cm$^{-2}$, (v) $p$-type $6.85 \times 10^{11}$ cm$^{-2}$, (vi) $p$-type $6.85 \times 10^{12}$ cm$^{-2}$, (vii) $p$-type $6.85 \times 10^{13}$ cm$^{-2}$, (viii) $p$-type $6.85 \times 10^{14}$ cm$^{-2}$. White lines indicate average Hartree potential $\langle V_H \rangle$, which aids in the visualization of band movements in the depletion zone. At lower doping levels, due to longer depletion regions, the length of the semiconductor side is increased from 100 to 300 Å. Transmission spectrum is presented for each case in the adjacent box on the same energy scale. Barrier heights are read from the difference between $E_F$ and onset of the transmission spectrum turn on (Tr onset). Yellow dashed lines in (iv) and (viii) denote the position of the metallurgical interface. (b) Distribution of MIGs at the Ag/$MoS_2$ interface. Projected DOS taken from first and second row of $MoS_2$ atoms at the interface. Density of mid-gap states is higher towards the valence band. (c) Relationship between barrier height and onset of transmission turn on. (i) At low doping, contacts are dominated by thermionic emission. In such contacts, onset of transmission corresponds one-to-one with the actual Schottky barrier. (ii) At intermediate doping, due to thinning of the Schottky barrier width, electrons can tunnel through the barrier at energies lower than the Schottky barrier. Tr onset will then deviate from the Schottky barrier. (iii) At very high doping levels, Schottky barrier itself can be lowered by doping and further increases the mismatch between Tr onset and actual barrier height. (d) Barrier heights vs doping density: as explained qualitatively for (b) and quantitively in SI.1 within the Supplemental Material [48], the barrier height will reduce as a function of doping. Therefore, we define the Schottky barrier height at the lowest possible doping where $n$-type and $p$-type barriers sum to 90% of the band gap. This point is usually achieved at doping levels of about $10^{11}$ cm$^{-2}$, which is also close to intrinsic defect doping of most 2D TMDs.

the Supplemental Material [48] for doping-dependent analysis of the Fermi-level pinning). This is also evident in Fig. 5(a), iv and vii, wherein, due to the presence of near-degenerate doping, a reduced Schottky barrier and band bending is observed (no band bending for the degenerate case, $6.85 \times 10^{14}$ cm$^{-2}$). As a consequence of these two effects, at high doping levels, the extracted $n$-type and $p$-type Schottky barriers no longer sum to the band gap of the TMD material. Therefore, the most logical approach to define a canonical Schottky barrier is to report the Schottky barrier at the lowest feasible doping level, where it is least affected by doping and where transmission-spectrum onset corroborates closely with the actual Schottky barrier, since thermally assisted tunneling current is negligible [Fig. 5(c), ii]. In our calculations, Schottky barriers are reported at $6.85 \times 10^{11}$ cm$^{-2}$, where the screening length of the depletion region is about 120 Å. It can be observed that, at this doping level, the extracted $n$- and $p$-type Schottky barriers sum to approximately 90% of the band gap [Fig. 5(d)], which shows that doping marginally affects the Schottky barrier, and there is no need to probe lower doping levels.

Using the transmission spectrum from NEGF simulations, by integrating over the contributions of available states at each energy level, an $I$-$V$ plot of the interface is calculated through the Landauer formula:

$$G = \frac{2q^2}{\hbar} \int T(E) \frac{\partial f}{\partial E} dE, \tag{1}$$

where $G$ is the device conductance without bias, $q$ is the elementary charge, $\hbar$ is the reduced Planck's constant, $T(E)$ is the transmission probability, and $f$ is the Fermi Dirac distribution function. The contact resistance is lastly extracted using the slope of the $I$-$V$ curve at zero bias [corresponding to $1/G(0)$] normalized by the cell's width. Furthermore, the temperature-dependent calculations are performed by evaluating the Fermi Dirac distribution function at various temperatures. Note that the contact resistances reported in this work are calculated at room temperature. Figure 6 shows the calculated $I$-$V$ curve for three different doping levels at various temperatures. At the lowest doping, all contacts exhibit typical Schottky behavior determined by thermionic emission over the barrier. This

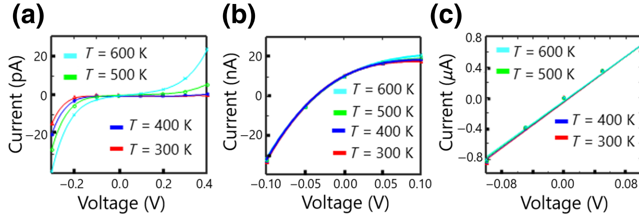


FIG. 6. $I$-$V$ curve at various temperatures ($T$). (a) At $N = 6.85 \times 10^{12}$ cm$^{-2}$; typical thermionic behavior. Due to doping, onset of reverse-bias tunneling current is small. (b) $N = 6.85 \times 10^{13}$ cm$^{-2}$; $I$-$V$ curve transitions towards more linear ohmic behavior. (c) $N = 6.85 \times 10^{14}$ cm$^{-2}$; fully ohmic behavior. Schottky barrier is transparent to tunneling current.

can be seen in both rectifying behaviors observed in the $I$-$V$ characteristics and from the temperature dependency of $I$-$V$. At intermediate doping, we observe that most contacts transition to thermionic field emission, where a swift turn on of the tunneling current in reverse bias is observed due to tunneling through the narrow Schottky barrier. Finally, at degenerate doping, tunneling through the barrier dominates transport and all contacts show completely linear and ohmic characteristics. It is worth mentioning that Fig. 6 represents the $I$-$V$ curve from an asymmetric system of a metal-semiconductor Schottky junction. However, in experiments, a realistic device would consist of metal-semiconductor-metal junctions that create two back-to-back Schottky diodes where one junction operates in reverse bias and the other in forward bias. Therefore, the actual 2D transistor response (metal-semiconductor-metal response) at low gate bias (subthreshold), resulting in low electrostatic channel doping, would be limited by the Schottky contact's reverse-bias (weaker) branch and exhibits symmetric behavior with respect to the drain-source voltage.

## III. RESULTS

### A. Electrical properties of edges

Figure 7(a) shows the extracted $n$-type and $p$-type canonical Schottky barriers for $MoS_2$ and five different metals at $\pm 6.85 \times 10^{13}$ cm$^{-2}$. Fitting the Schottky barriers and their associated error bars with the pinned Schottky-barrier model [Fig. 3(b)], our results suggest that the $MoS_2$ edge contact is pinned to a CNL that lies approximately 665 meV (595–735 meV error margin) above the valence band. Given that this margin is moderately lower than the mid gap, this suggests overall $p$-type behavior. This contrasts with 2D $MoS_2$ top contacts, where the CNL usually lies closer to the conduction band. Notably, the anisotropy between the $n$-type CNL for top contacts and the $p$-type CNL for edge contacts was also predicted by Guo et al. [75]; this was inferred from the difference between the average energies of orbitals that were relevant to either

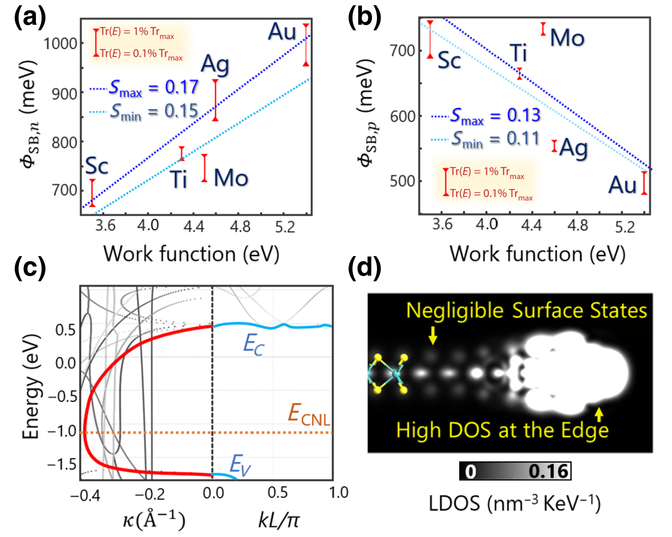


FIG. 7. Fermi-level pinning analysis in edge contacts. (a) $n$-Type Schottky barrier vs the metal's work function. (b) $p$-Type Schottky barrier vs the metal's work function. The error bar for Schottky barriers is extracted by choosing two different thresholds of $T(E)$ as the definition for the onset of transmission turn on. The upper limit is set by the energy at which transmission reaches 1% of maximum transmission and the lower limit is set by energy at which $T(E)$ arrives at 0.1% of maximum transmission. (c) Complex band structure of 1$L$-$MoS_2$ along the in-plane direction. The branching point corresponds to a CNL of 715 meV measured from top of the $E_V$. (d) Local density of states of terminated Mo-ZZ-2S edge of $MoS_2$ showing a high density of the terminated states compared to the top interface.

edge or top conduction. To summarize, the Mo orbitals with symmetry bonding along the cross-plane direction, namely, $d_{z^2}$, $d_{x^2-y^2}$, and $d_{xy}$, that are responsible for top injection are distributed equally along the valence and conduction bands with energies averaging near the mid gap. The Mo states with symmetry bonding along the in-plane direction, $d_{xz}$ and $d_{yz}$, have higher densities in the valence band and result in a CNL closer to the valence band.

The CNL of the edge contacts can also be approximated from the branching point of the complex band structure along the transport direction perpendicular to the Mo ZZ interface. The complex band structure represents the dispersion of evanescent solutions of the Schrodinger's equation, which occupies mid-gap energies when the translational symmetry of the crystal is broken by the interface. In the virtual induced-gap-states model [47,76], the energy that separates the donorlike and acceptorlike mid-gap states is the energy where the penetration length of the evanescent waves reaches its minimum ($E_{k,\max}$) and is called the branching point. In the absence of additional interface-state contributors, such as defects and adatoms, branching points will also represent the charge-neutrality level. From Fig. 7(c), the branching point can be extracted

at $E_B = \sim 715$ meV, which correlates relatively well with the extracted CNL from Fig. 7(b).

Furthermore, the pinning factor for both the $n$-type ($S = 0.15-0.17$) and $p$-type edge contacts ($S = 0.1-0.13$) also suggests stronger pinning compared with the theoretical values for pristine top contacts ($S = 0.3-0.7$) [the degree of pinning for top contacts ($S$ factor) heavily depends on the fabrication method. For instance, in evaporated or transferred top contacts, almost ideal $S$ factors, close to one, are observed. These results are consistent with DFT simulations in which the metal preserves a manually fixed large vdW gap. But, when in DFT simulations the metal is allowed to geometrically relax on top of the TMD, the $S$ factor is no longer ideal and varies between 0.3 and 0.7] [20,75,77]. This is to be expected, as the broken periodicity along the in-plane direction warrants a high density of dangling bonds and evanescent edge states compared with the out-of-plane direction [Fig. 7(d)]. Also, the marginally stronger pinning factor for the $p$-type Schottky barrier can be attributed to the higher distribution of mid-gap states toward the valence band [see Fig. 5(b)]. One should note that the interface states present in our calculations solely originate from the terminated edge states of the semiconductor. There is a possibility that, similar to top contacts, additional prevalent defect complexes in edge contacts form and alter this result. Hence, the results are only valid for atomically abrupt edge contacts.

Figures 8(a) and 8(b) show the extracted contact resistance versus doping of $MoS_2$-terminated edge with five different metals. As predicted, at lower dopings ($N < 10^{13}$ cm$^{-2}$), the Schottky barrier completely dominates conduction and metals with lower (higher) work functions repeatedly yield better $n$-type ($p$-type) contacts. Furthermore, at low doping levels ($N < 10^{13}$ cm$^{-2}$), almost all metals (except for scandium) show lower $p$-type contact resistance due to the positioning of the CNL. At intermediate dopings, $10^{13} < N < 10^{14}$ cm$^{-2}$, contacts transition to thermionic field emission and contact resistances drop significantly. In a doping region at about $6.85 \times (10^{13}-10^{14}$ cm$^{-2})$, the contacts become completely ohmic, with surprisingly low $R_c$ (<40 $\Omega\,\mu$m), well below the IEEE International Roadmap For Devices and Systems (IRDS) requirements [27]. It is notable that, at higher dopings, contacts become less sensitive to the metal work function, and the dominating factor that determines the contact resistivity becomes the total number of available modes with matching **k** vectors [78] and their transmission probability across the interface. For instance, it is observed that, at very high dopings, while both $n$-type and $p$-type barriers are negligible, the $p$-type contact resistances are, on average, lower than the $n$-type contacts. Again, this can be ascribed to the higher density of states of in-plane modes in the valence band of $MoS_2$, as discussed in Sec. III.

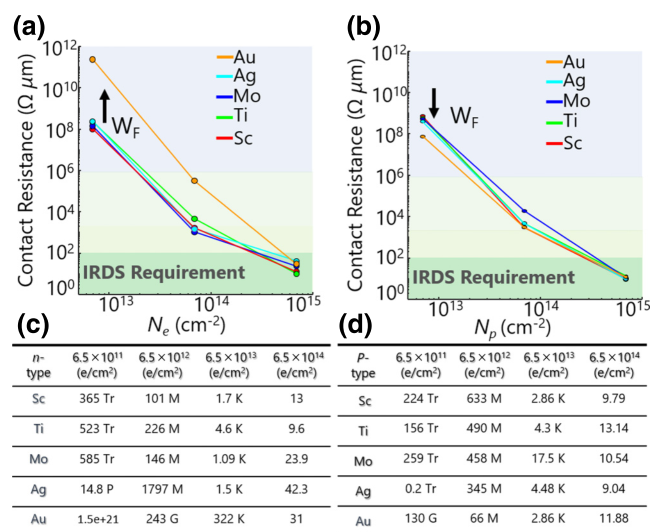


| $n$-type | $6.5\times10^{11}$ (e/cm$^2$) | $6.5\times10^{12}$ (e/cm$^2$) | $6.5\times10^{13}$ (e/cm$^2$) | $6.5\times10^{14}$ (e/cm$^2$) |
|---|---|---|---|---|
| Sc | 365 Tr | 101 M | 1.7 K | 13 |
| Ti | 523 Tr | 226 M | 4.6 K | 9.6 |
| Mo | 585 Tr | 146 M | 1.09 K | 23.9 |
| Ag | 14.8 P | 1797 M | 1.5 K | 42.3 |
| Au | 1.5e+21 | 243 G | 322 K | 31 |

| $P$-type | $6.5\times10^{11}$ (e/cm$^2$) | $6.5\times10^{12}$ (e/cm$^2$) | $6.5\times10^{13}$ (e/cm$^2$) | $6.5\times10^{14}$ (e/cm$^2$) |
|---|---|---|---|---|
| Sc | 224 Tr | 633 M | 2.86 K | 9.79 |
| Ti | 156 Tr | 490 M | 4.3 K | 13.14 |
| Mo | 259 Tr | 458 M | 17.5 K | 10.54 |
| Ag | 0.2 Tr | 345 M | 4.48 K | 9.04 |
| Au | 130 G | 66 M | 2.86 K | 11.88 |

FIG. 8. Lower limits of edge $R_c$. (a) Contact resistances for $n$-type contacts. (b) Contact resistances for $p$-type contacts. Values are extracted at 300 K. (c) Data points for $n$-type contacts. (d) Data points for $p$-type contacts.

We should emphasize that our ballistic simulation framework does not consider dissipative mechanisms, such as electron-phonon, remote phonon, and defect scatterings. Moreover, in practical applications, most doping mechanisms, such as substitutional doping, will also inevitably introduce detrimental effects, such as additional impurity scattering pathways and reduced gate electrostatic control. Therefore, the values reported in this work should be treated as a theoretical upper limit to the electrical performance of the analyzed interfaces. Finally, the high doping concentrations assumed in this work are on a par with state-of-the-art CMOS technologies, which are not yet developed for 2D material platforms. Furthermore, in the immediate future, achieving such doping concentrations solely through the usual gating method would face challenges such as dielectric breakdown and excessive gate leakage. Therefore, as discussed in Sec. IV, it is essential to study other mitigating solutions to reduce the Schottky barrier.

Revisiting Figs. 7(a), 7(b) and 8, it seems that only the Mo contact diverges from the work-function trend. Taking a closer look at the contact interface between Mo-ZZ-2S and Mo, it becomes evident that this interface naturally resembles the interface of bare $MoS_2$ ZZ termination with a contact metal without sulfur dimers. This encourages us to analyze the effect of the existence of sulfur passivation in more detail.

### B. Effect of sulfur edge passivation

To analyze the effect of the termination edge in-depth, we also carry out our analysis for $MoS_2$ with purely Mo-terminated zigzag edges (see SI.5 within the Supplemental

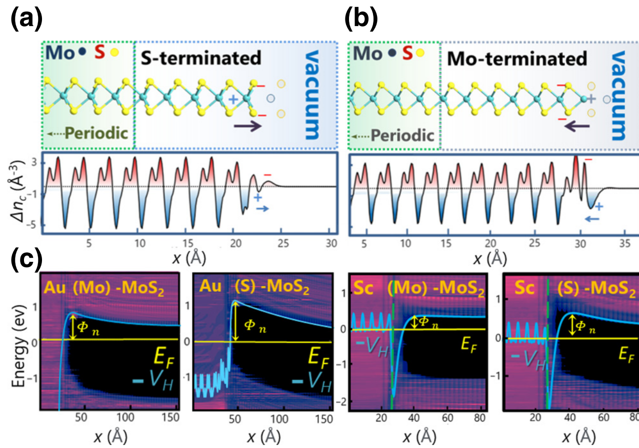


FIG. 9. Effect of sulfur passivation on contact resistance. (a) S-terminated $MoS_2$-ZZ-2S and (b) Mo-terminated $MoS_2$-ZZ-bare interfaces. Due to the polar nature of Mo—S bonds, two different dipoles form at the edge of different zigzag-terminated $MoS_2$. Bottom inset figures show the in-plane average electron difference density (EDD), which indicates the formation of dipoles with opposite polarities at the edge. Positive EDD represents electron accumulation and negative EDD represents electron depletion. In S termination, dipole will increase effective work function of the edge, pulling bands upward, while in Mo termination, dipole reduces effective edge work function and pulls bands downward. (c) PLDOS of S- or Mo-terminated $MoS_2$ with Au and scandium. Outcome of different termination edges is best seen by comparing actual barriers formed in the two different termination cases. Evidently, Mo termination results in lower *n*-type Schottky barriers compared with S terminations. This trend holds true for all simulated interfaces. (Here, only Au and Sc are shown, since they represent both ends of the work-function spectrum. See SI.5 within the Supplemental Material [48] for all results.)

Material [48]). While Mo-terminated edges without sulfur dimers may not be the most thermodynamically stable edge formation of $MoS_2$, but it is still possible to engineer such interfaces using either *in situ* growth [41] or additional annealing steps [79]. We can observe that, in contrast to Mo edges with sulfur passivation [Fig. 9(a)], bare Mo-terminated edges [Fig. 9(b)] repeatedly demonstrate lower (higher) *n*-type (*p*-type) Schottky barriers [Fig. 9(c)]. Therefore, one can conclude that the charge-neutrality level for bare $MoS_2$ ZZ edges places above the CNL for sulfur-passivated interfaces and is closer to the mid gap and more ambipolar than sulfur-terminated edges. This effect can be attributed to the polarity of Mo—S bonding, which results in different charge redistribution at the cleaved interface [Fig. 9(b)].

### C. Edge contacts vs top contacts

At this point, we observe that edge contacts offer lower *p*-type Schottky barriers compared with top-contact geometry. This already suggests that, if the transmission rates (normalized with respect to the Fermi-level) for edge contacts are not substantially different from the top contacts, they will have the ability to outperform top contacts in hole conduction. At first sight, one might think that it is not appropriate to compare lateral edge contacts to top contacts as the active atomically thin interface area for edge contacts is constant and much smaller than what can be achieved in top contacts. This concern is valid. Indeed, if transmission increases as the overlap area increases for top metals, then one cannot compare top contacts to edge contacts on equal footing. In essence, the question returns to whether conduction or injection in top contacts occurs throughout an effective area or happens solely at the edge of the top metal. Prakash *et al*. [80] utilized two injection mechanisms to model the 2D metal contacts, path 1, as denoted in Fig. 10(a), presents the path through which the electron is injected from the metal to the 2D channel underneath (areal injection), and path 2 is where the electron is injected to the semiconductor at the edge of the metal.

Recent findings [35,36] suggest that, as the channel thickness is thinned down, for monolayer 2Ds, conduction via path 1 (under the metal) is heavily suppressed and that the actual effective injection occurs solely at the edge of the metal (path 2). Our simulations corroborate these results. This is best understood by comparing the qualitative band profiles of different injection mechanisms in monolayer and multilayer TMDs. For multilayer TMDs, the depletion region along path 1 has sufficient space to screen the potential in the vertical direction [see *A*-*B* in Fig. 10(a), i]. Therefore, in the reverse-bias region, electrons using thermally assisted tunneling can conduct through the Schottky barrier to the semiconductor under the metal and flow laterally to the electrode. However, in the monolayer limit, the Schottky-barrier potential is barely screened in the vertical direction [see *A*-*B* in Fig. 10(a), ii] and the Fermi level inside the semiconductor is pinned to a level determined by the top metal's Fermi-level pinning [77]. In this case, electrons can no longer tunnel to the metal underneath, since there are no available states in the semiconductor at the same energy. Hence, in the monolayer limit, conduction via path 1 is suppressed, but conduction through path 2 remains the same for both monolayer and multilayer semiconductors [see edge-injection band alignment in Fig. 10(a)], and the total current becomes dominated by edge injection (path 2) for the monolayer. Notably, the ratio of the contribution between path 2 and path 1 will depend on $V_{DS}$, the Fermi-level pinning position of the top contact, and the type of gate.

One should also note that this analysis is only valid when the contact is reverse biased. If the contact is in the forward-bias region, the total current through the device is dominated by thermionic emission, which implies that there will be no difference between path 1 and path 2. This can be seen in Fig. 10(b), ii–iii, where we present the current density across the top-contact device. Given that

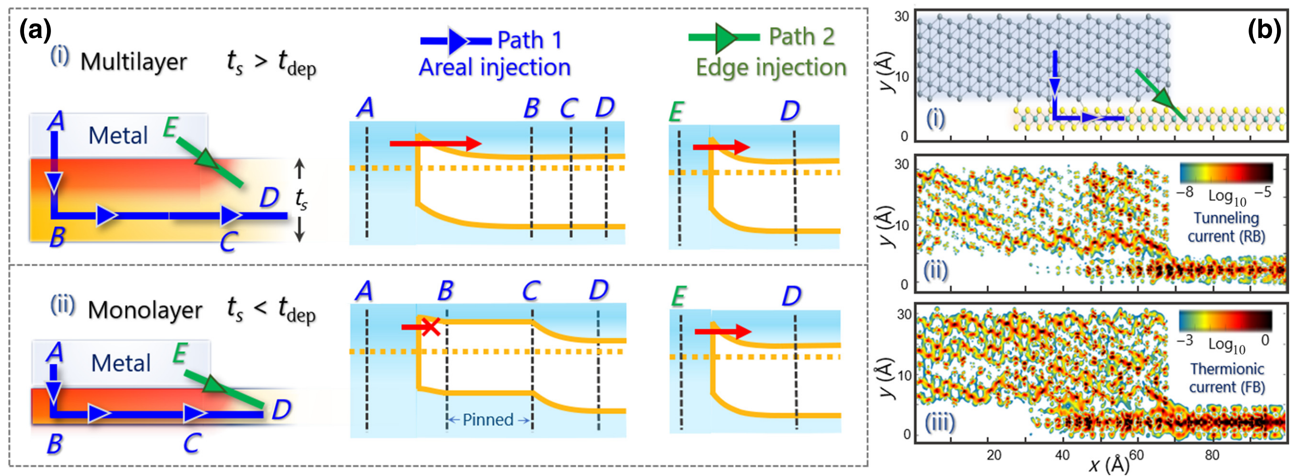


FIG. 10. Current injection pathways in monolayer and multilayer limit. (a) Qualitative band diagrams for injection mechanism in multilayer and monolayer limits. Electron injection can generally be categorized as either injection through the edge of the metal, aka edge injection (green arrow), or injection to the overlapping semiconductor (blue arrow). Red region denotes the depletion region of the semiconductor. (i) When the thickness of the semiconductor is larger than the depletion length, there is no difference between the barrier from path 1 and path 2. (ii) For very thin semiconductors, such as monolayer $MoS_2$, the Schottky-barrier potential is barely screened in the vertical direction ($A$ to $B$). Fermi level of the semiconductor under the metal is pinned to a level determined by the top metal (region $B$-$C$) and semiconductor under the metal can be considered fully depleted. In this case, the electron cannot tunnel to the overlap region, since there are no available states and effectively the areal current will be suppressed. However, the barrier to path 2 remains untouched. (b) Current density plots for Au-$MoS_2$ ($1L$) top contacts with $N = 6.85 \times 10^{12}$ cm$^{-2}$: (i) atomic configuration of the interface. (ii) Current density plot at the onset of transmission turn on for the reverse-bias junction ($V_{RB} = 0.3$ V). Tunneling current occurs through path 2 and is suppressed under the metal. (iii) Current density plot at the onset of transmission turn on for a forward-bias junction ($V_{FB} = 0.1$ V). Thermionic current flows through both path 1 and path 2.

the reverse-bias junction is the limiting factor to contact resistance of the total device, we can conclude that, for monolayer TMDs, it is fair to compare edge and top contacts, as in both effective injections occur across the edge of the metal.

To test this hypothesis and compare the edge contacts to pristine top contacts, we simulate top and edge contact formations between $MoS_2$ and Au using the same framework presented earlier (see SI.6 within the Supplemental Material [48] for simulation details). As expected, the top contact between Au and $MoS_2$ yields a smaller (larger) $n$-type ($p$-type) barrier with respect to edge contacts due to the difference in the CNL of top interfaces [Fig. 11(c)]. Extracted contact resistances [Figs. 11(a) and 11(b)] demonstrate that, at the same doping level, the edge contacts can surpass top contacts by over an order of magnitude due to the lower Schottky barrier. However, edge contacts cannot outperform top contacts in electron conduction. These results suggest that any enhancement in transmission rates in edge contacts that might occur due to the elimination of the vdW barrier has a marginal effect on contact resistance. In fact, the charge redistribution caused by strong covalent bonding at the edge interface more strongly pins the Fermi level to energies below the mid gap [Fig. 11(d)], which hinders $n$-type electron transport. It is readily observable that the effect of this pinning far exceeds any improvement to contact resistance due to elimination of the vdW gap.

### D. Schottky-barrier inhomogeneity, hybrid contacts, and the effect of imperfect edge formations

At first glance, inhomogeneity between Fermi-level pinning at the edge and top interface appears to be an excellent opportunity to achieve both $n$-type and $p$-type low-contact resistances by simultaneously contacting both edge and top interfaces in a "hybrid contact" scheme, as illustrated in Fig. 12(a). Here, we argue that such hybrid contacts may only be advantageous in contacts to multilayer TMDs. Notably, the formation of such hybrid contacts, with a metal overlap on the top TMD surface, is also highly likely to happen unintentionally during the fabrication of edge contacts using the $h$-BN encapsulation technique. This is because, to expose the TMD edge, the $h$-BN/TMD stack must be etched at an angle that will inadvertently expose some of the TMD surfaces as well (imperfect edge contacts).

To comprehend the effect of the overlapping metal in hybrid contacts, we further study the interface of

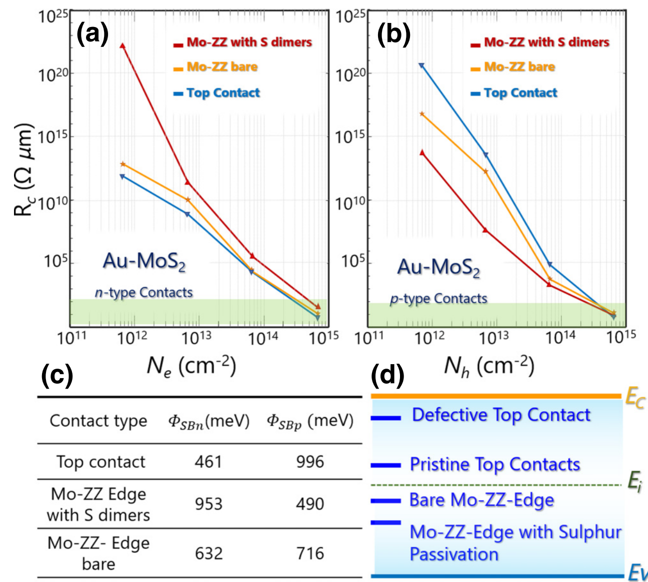


| Contact type | $\Phi_{SBn}$(meV) | $\Phi_{SBp}$ (meV) |
|---|---|---|
| Top contact | 461 | 996 |
| Mo-ZZ Edge with S dimers | 953 | 490 |
| Mo-ZZ- Edge bare | 632 | 716 |

FIG. 11. Performance of Au-$MoS_2$ edge contacts vs top contacts. (a) Electron injection, $R_c$ vs electron density; (b) hole injection, $R_c$ vs hole density. (c) Comparison of measured Schottky barriers. (d) Qualitative sketch illustrating the Fermi-level pinning in different contact geometries.

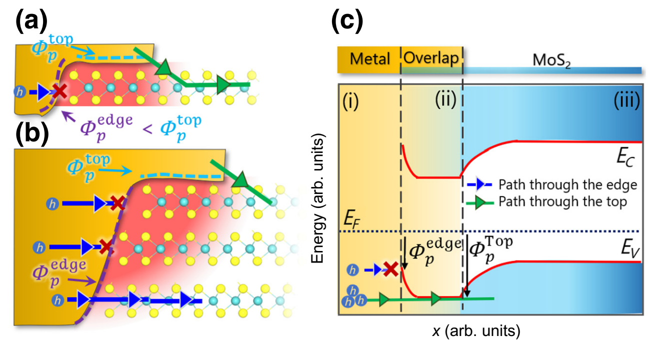


FIG. 12. Hybrid contacts and exploiting Schottky-barrier inhomogeneity. (a) Schematic representation of hybrid contact to monolayer $MoS_2$. Red area denotes the depletion region. Purple dashes represent the edge interface where the low hole barrier is caused by Fermi-level pinning at the edge. Cyan blue dashes represent the top interface where the high hole barrier or low electron barrier is caused by Fermi-level pinning at the top surface. Depletion region created by Fermi-level pinning from the top surface of the contact prohibits conduction of holes from the smaller $p$-type barrier at the edge, raising the effective hole barrier from the edge to the same value as the top surface. (b) Schematic representation of hybrid contacts to multilayer $MoS_2$. Screening of the depletion region now allows holes to conduct through the lower $p$-type barrier of the edge at lower layers. (c) Schematic band alignment of hybrid contact to monolayer $MoS_2$. Fermi level in the semiconductor under contact, region (ii), is governed by Fermi-level pinning of the top contact. In the meantime, TMD edge, the boundary between region (i) and (ii), still retains its low $p$-type Schottky barrier; however, effective barrier for holes at the edge (blue arrow) is increased by $n$-type pinning of the top contact in region (ii).

Au-monolayer-$MoS_2$ hybrid contacts [Fig. 12(a)] using the established framework (see SI.7 within the Supplemental Material [48] for details). Figure 12(c) shows the overall band alignment of a hybrid contact between Au and $MoS_2$ ($p$-type configuration). It is observed that the Schottky barrier at the edge still retains its dominant $p$-type behavior. However, holes still cannot enter the semiconductor at the lower Schottky barrier in the edge (represented by blue arrows), since the potential inside the semiconductor immediately after the edge is pinned to a lower value by the Fermi-level pinning effect of the top metal. This increases the effective $p$-type barrier that is determined by the top metal. Notably, this effect is again caused by the marginal screening of the semiconductor's potential in the vertical direction (depletion region due to the top contact is depicted as the red region) similar to edge-injection effects in Fig. 10(a), ii. As the number of layers increases and the depletion width is screened in the vertical direction under the metal [Fig. 12(b)], the top metal no longer affects the barrier for holes in the edge interfaces of bottom $MoS_2$ layers and, therefore, holes can now conduct at lower Schottky-barrier energies for the edge. Therefore, these types of hybrid contacts (or imperfect edge contacts) will have dominant $n$-type behavior at the monolayer limit (as the Schottky barrier is dominated by the lower $n$-type Schottky barrier for top contacts) and, as the thickness of the 2D flake is increased, the contact becomes dominantly $p$ type. This trend was also observed in recent experimental studies [40,43], where it was attributed to weak Fermi-level pinning at the edge; here, we argue that it could be explained as a consequence of inhomogeneous Schottky barriers at the edge and top interfaces. Overall, our results demonstrate that, in the monolayer limit, to leverage the low $p$-type Schottky barrier at the edge contact, the junction must become as abrupt as possible with a minimum overlap area. Another way to circumvent this limitation and to leverage the Schottky-barrier inhomogeneity for $n$-type and $p$-type conduction is to use multilayer (3D) source-drain regions, while maintaining the channel atomically thin. We describe this approach more in-depth in Sec. IV.

### E. $MoS_2$-graphene lateral contact and dynamic reduction of the Schottky barrier

Our analysis until this point has primarily focused on interfaces of conventional bulk (3D) materials with 2D $MoS_2$. However, a research opportunity has been made available in the realm of 2D graphene lateral heterojunctions. This approach is inspired by the concept of seamless or edge-contacted all-2D circuits [33,81]. 2D graphene lateral contacts offer a unique advantage over traditional 3D-2D edge contacts in that their Schottky barrier can be

modulated via gate electrostatics, an effect we call dynamic control of the Schottky barrier. Graphene is a semimetal with low DOS near the Dirac point (low quantum capacitance). Therefore, upon application of an electric field, to accommodate for the accumulated charge, the Fermi level in graphene moves to higher or lower energies (depending on the gate polarity), which effectively changes graphene's work function [Fig. 13(a)]. This effect can be leveraged in device designs where the gate overlaps with the graphene-TMD interface [Fig. 13(b)] to allow for a dynamic reduction in the Schottky barrier as the device is turned on [82]. To simulate this effect, we use an in-house NEGF code [4] based on a tight-binding model to solve the NEGF and Poisson's equation iteratively to obtain the potential distribution, local density of states, and the carrier density for graphene-$MoS_2$-graphene lateral heterostructure (see SI.8 within the Supplemental Material [48] for more details). In the simulation domain, the gate not only covers the channel, but also overlaps with the graphene interface to mimic electrostatic gating. Figure 13(c) represents the simulated LDOS and band diagram of a graphene-$MoS_2$-graphene device with an applied gate voltage. It is readily observable that, due to the low DOS of graphene, the Dirac point in graphene is pulled down close to the interface, leading to a smaller $n$-type Schottky barrier with respect to the off state. High-conductivity graphene, which also helps to reduce the series resistance of the graphene-$WS_2$-graphene heterostructure in field-effect transistor applications, along with a dynamically tunable Schottky barrier has shown a record-breaking on current with contact resistances as low as 0.67 k$\Omega$ $\mu$m [82].

The synthesis of graphene-TMD lateral heterostructures is usually done by carving out a window in graphene proceeded by the growth of TMD from graphene's edge-nucleation sites using chemical vapor deposition or metalorganic chemical vapor deposition techniques. Interestingly, the morphology of the graphene-TMD interface is not an abrupt atomic junction, but, as repeatedly demonstrated [82–85], an effective overlap area is created on top of graphene by the TMD. This overlap can be as small as 2 nm based on growth conditions. Hence, technically the synthesized graphene-TMD lateral heterostructures are not pure edge contacts and more in line with a hybrid- or top-contact configuration.

The degree of the performance boost from work-function modulation is directly proportional to the pinning factor of the graphene-TMD interface (at intermediate doping levels, where the contact is determined by thermionic or thermally assisted field emission). For instance, at a true Schottky-Mott limit ($S = 1$), the Schottky-barrier modulation effect should theoretically yield high-performance ambipolar transistors. However, due to the presence of intrinsic defects in TMDs, Fermi-level pinning is inevitable in most experimental demonstrations, and fabricated devices demonstrate a strong mode mismatch.

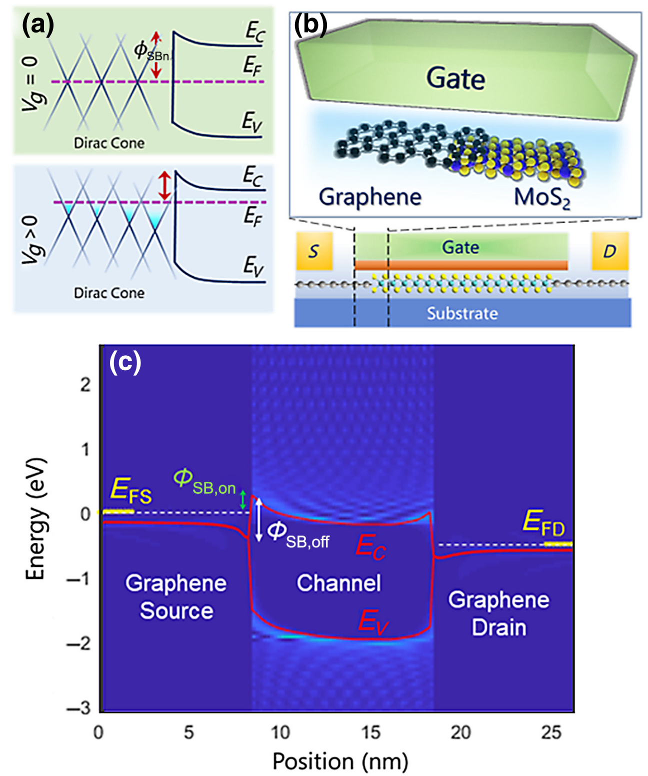


FIG. 13. Dynamic reduction of Schottky barrier. (a) Qualitative band alignment of graphene-$MoS_2$ Schottky barrier. (b) Gated graphene-$MoS_2$ interface in a lateral graphene-$MoS_2$ FET. (c) LDOS plot of graphene-$MoS_2$-graphene heterostructure with applied gate. As the gate turns on, Fermi level in graphene moves to higher energy and its work function is lowered, which results in a reduction of Schottky barrier height.

However, recently, Cao *et al*. [86], leveraging the band alignment between graphene and $WSe_2$, have been able to demonstrate a balanced gate-tunable ambipolar TMD transistor without mode mismatch.

Overall, graphene-TMD heterostructures, with their potential for large-scale manufacturability [82,87], high interfacial thermal conductivities [88], and dynamically tunable Schottky barriers, show a promising path toward the realization of high-performance devices in the near future.

## IV. OUTLOOK

It should be emphasized that the interfaces under study are purely defect-free interfaces. Similar to the presence of defect complexes in 2D top contacts, which govern electrical conduction through the top, electrical properties of edge contacts can also be susceptible to inevitable defect formations at the edge. Further *ab initio* simulations and experimental characterizations are required to identify probable defect complexes that may occur in different edge-contact fabrication techniques. Furthermore,

strong Fermi-level pinning caused by covalent bonding in the pristine edge contacts will hinder their contact resistances in the near future, since no reliable doping technology has yet been developed for 2D TMDs. In the meantime, it might be advantageous to explore other unorthodox solutions. For instance, the application of intercalation [18,89–92] can be a promising pathway to degenerately dope the area adjacent to metal contacts. Moreover, edge contacts do not necessarily have to form between pristine $2H$-phase TMDs and contacting metals. Phase engineering methods, such as converting $2H$-phase $MoS_2$ to $1T$ phase in the immediate contact region [93], have shown promise in improving contact properties. Such phase engineering methods can also be utilized for edge contacts as an alternative to degenerate doping, if the metallic phase can be made stable. Approaches such as roughness engineering can be used to increase the edge length or contact-area ratio to achieve lower contact resistance [20]. Meanwhile, graphene-TMD edge contacts have shown the best overall performance, which is attributed to their unique contact-gating properties [82].

As mentioned earlier, the range of achieved contact resistances in demonstrations of edge contacts varies by over 4 orders of magnitude with a few seemingly contradictory results. For instance, Choi [40] and Moon [39] have reported dominant $n$-type behavior in Au-$MoS_2$ edge contacts, whereas Yang *et al.* [43] have reported strong $p$-type behavior in Au-$MoS_2$ edge contacts. Intriguingly, both $n$-type Schottky barriers of less than 50 meV and $p$-type negative Schottky barriers have been reported in Au/$MoS_2$, even though the contact resistances are in the $\mathrm{M}\Omega\,\mu$m range. This apparent contradiction between measured Schottky barriers and contact resistances is attributed to the atomically narrow one-dimensional active cross section of the $MoS_2$ edge; however, as shown in this work and other experimental papers [93], contact resistances as low as 200 $\Omega\,\mu$m are achieved solely through edge contacts to $MoS_2$; therefore, the limited active cross section in itself cannot be the sole reason. Yang *et al.* [43] have argued that edge contacts perform close to the Schottky-Mott limit ($S = 1$); however, results from the groups of Cheng, Yang, and Moon, in which Au-$MoS_2$ and Ni-$MoS_2$ contacts (the Au and Ni work functions are 5.4 and 5.2 eV respectively, which should yield strong $p$-type contacts) show a dominant $n$-type branch that is not to be expected. It is evident at this point that the specific interface atomic configuration of different edge-contact demonstrations varies from method to method. While our analysis of imperfect edge contacts in this manuscript can justify some of these apparent contradictions, such as the $n$-type to $p$-type dominant transition of Au-$MoS_2$ edge contacts with increased thickness of the TMD flake, further experimental TEM and STEM characterizations are needed to shed light on the atomic morphology of the edge interfaces achieved via different fabrication methods. The formation of depinning oxide layers and strain-induced $1T$' phases [94] is also probable and can justify some of these experimental observations. Furthermore, care must be taken when applying the flat-band Schottky-barrier extraction method [58] to 1D contacts. It should be emphasized that estimating the Schottky barrier from the flat-band condition is only viable when the gate has not reached the threshold voltage, which can lead to a misconstruction of negative Schottky barriers as elucidated in [21]. Finally, during the analysis of the Schottky barrier using the flat-band method, the exact power of the temperature term relative to the number of layers exists in a gray area, which can introduce uncertainties into the extracted results. In the future, electro-optical Schottky-barrier measurement techniques must be employed to circumvent these problems and optimize the all-electrical flat-band measurement methods to yield more accurate estimations.

Finally, it is important to emphasize that the suppression of the areal-injection current mechanism [Fig. 10(b)] in contacts to monolayer TMDs indicates that these contacts are much more susceptible to current-crowding effects. It is still unclear to what extent such current-crowding effects, which can impact the device's self-heating and performance, and thereby chip-scale power dissipation and reliability of nanoscale ICs [95], complicate the future 2D transistor architectures. Further studies are required to ascertain how semiconductor doping is able to relieve potential current-crowding effects. However, a design consideration can be derived to alleviate this problem, which is to use the 3D (multilayer) source-drain region, while keeping the channel monolayer (Fig. 14), to allow sufficient space for screening of the Schottky-barrier potentials near the source-drain electrodes. This design, in effect, allows for areal-current injection pathways, which can relieve contact resistance during potential current-crowding scenarios. Moreover, the hybrid design of the contact allows for possible complimentary device operation of a 2D FET. This is achievable since the $n$-type Schottky barrier for the top contact is approximately on the same order as the $p$-type Schottky barrier for edge contact (See Fig. 11). Therefore, in NMOS operation (devices made using $n$-type intercalants), current takes the least resistive path through the top contact and in PMOS operation (devices made using p-type intercalants), current takes the least resistive path through the edge. An interesting addendum to this design is that the multilayer source-drain regions are suitable for intercalation doping [90–92], whereas the monolayer channel, due to its thickness, can be engineered to remain unaffected by intercalation processes. Several technological problems must be addressed to make this type of design feasible. First, etching the channel down to a monolayer is a challenging task using conventional etchants. Atomic layer etching or novel 2D TMD device fabrication techniques must be perfected to achieve this capability. Furthermore, the reliability and stability of the

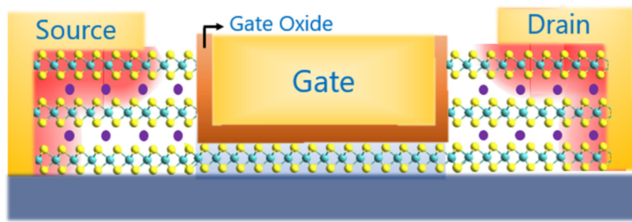


FIG. 14. Proposed 2D FET with raised intercalated source-drain. Purple dots denote foreign intercalant agents that dope the source-drain region. For NMOS devices, *n*-type intercalants are used, and for PMOS devices, *p*-type intercalants can be used. Red shades denote the boundary of the Schottky barrier width. 3D nature of the source-drain maximizes available electron-injection pathways compared with limited narrow injection paths in regular 1*L* 2D FETs. Moreover, this design can leverage Schottky-barrier inhomogeneity of top and edge interfaces to achieve complimentary operation.

selective-area intercalation process must be studied to assess their manufacturability.

## V. CONCLUSION

Our results show that 1D edge contacts to 2D monolayer $MoS_2$ are typically dominated by a *p*-type conduction mechanism due to the placement of their charge-neutrality level close to the valance band. Moreover, we can observe that bare Mo-ZZ-terminated edge contacts can achieve better *n*-type contacts compared with sulfur-passivated Mo-terminated contacts. At typical experimentally achievable doping levels, 1D edge contacts can supersede the top contact in *p*-type conduction and achieve lower contact resistances, despite their atomically thin overlap. Furthermore, we reveal that, as a consequence of Schottky-barrier inhomogeneity between the top and edge interfaces, it is essential to achieve abrupt 2D-2D lateral junctions without any metal overlap to utilize the lower *p*-type Schottky barrier in edge contacts. Nevertheless, from a practical perspective, the dynamic tunability of the Schottky-barrier at the graphene-TMD lateral heterojunctions, which leverages some overlap between graphene and TMD, provides an interesting case study. Likewise, FETs with 3D raised source-drain geometries are preferred, which can leverage this Schottky-barrier inhomogeneity, while maximizing the available current-injection pathways, thereby enabling 2D FETs to achieve their true predicted potential as well as complimentary operation without changing the source and/or drain contact metal.

## ACKNOWLEDGMENTS

This research is supported by the ARO (Grant No. W911NF1810366) and the Japan Science and Technology Agency (JST) Core Research for Evolutional Science and Technology (CREST) Program under Grant No. SB180064. Use is made of computational facilities purchased with funds from the National Science Foundation (Grant No. CNS-1725797) and administered by the Center for Scientific Computing (CSC). The CSC is supported by the California NanoSystems Institute and the Materials Research Science and Engineering Center (MRSEC; NSF DMR Grant No. 1720256) at UC Santa Barbara.

[1] K. S. Novoselov, *et al.*, Two-dimensional atomic crystals, Proc. Nat. Acad. Sci. USA **102**, 10451 (2005).

[2] B. Radisavljevic, A. Radenovic, J. Brivio, V. Giacometti, and A. Kis, Single-layer $MoS_2$ transistors, Nat. Nanotechnol. **6**, 147 (2011).

[3] Y. Yoon, K. Ganapathi, and S. Salahuddin, How good can monolayer $MoS_2$ transistors be?, Nano Lett. **11**, 3768 (2011).

[4] W. Cao, J. Kang, D. Sarkar, W. Liu, and K. Banerjee, 2D semiconductor FETs - projections and design for Sub-10 nm VLSI, IEEE Trans. Electron Devices **62**, 3459 (2015).

[5] S. Kim, *et al.*, High-mobility and low-power thin-film transistors based on multilayer $MoS_2$ crystals, Nat. Commun. **3**, 1011 (2012).

[6] J. Jiang, K. Parto, W. Cao, and K. Banerjee, Ultimate monolithic-3D iintegration with 2D materials: Rationale, prospects, and challenges, IEEE J. Electron Devices Soc. **7**, 878 (2019).

[7] D. Xiao, G. Bin Liu, W. Feng, X. Xu, and W. Yao, Coupled Spin and Valley Physics in Monolayers of $MoS_2$ and Other Group-VI Dichalcogenides, Phys. Rev. Lett. **108**, 1 (2012).

[8] K. F. Mak, K. He, J. Shan, and T. F. Heinz, Control of valley polarization in monolayer $MoS_2$ by optical helicity, Nat. Nanotechnol. **7**, 494 (2012).

[9] K. F. Mak, K. L. McGill, J. Park, and P. L. McEuen, The valley hall effect in $MoS_2$ transistors, Science **344**, 1489 (2014).

[10] J. R. Schaibley, *et al.*, Valleytronics in 2D materials, Nat. Rev. Mater. **1**, 16055 (2016).

[11] K. He, C. Poole, K. F. Mak, and J. Shan, Experimental demonstration of continuous electronic structure tuning via strain in atomically thin $MoS_2$, Nano Lett. **13**, 2931 (2013).

[12] P. Rivera, *et al.*, Observation of long-lived interlayer excitons in monolayer $MoSe_2$-$WSe_2$ heterostructures, Nat. Commun. **6**, 4 (2015).

[13] K. Tran, *et al.*, Evidence for moiré excitons in van der Waals heterostructures, Nature **567**, 71 (2019).

[14] Y. M. He, *et al.*, Single quantum emitters in monolayer semiconductors, Nat. Nanotechnol. **10**, 497 (2015).

[15] M. Toth and I. Aharonovich, Single photon sources in atomically thin materials, Annu. Rev. Phys. Chem. **70**, 123 (2019).

[16] D. Chimene, D. L. Alge, and A. K. Gaharwar, Two-Dimensional nanomaterials for biomedical applications: Emerging trends and future prospects, Adv. Mater. **27**, 7261 (2015).

[17] D. Sarkar, W. Liu, X. Xie, A. C. Anselmo, S. Mitragotri, and K. Banerjee, $MoS_2$ field-effect transistor for next-generation label-free biosensors, ACS Nano **8**, 3992 (2014).

[18] P. Ajayan, P. Kim, and K. Banerjee, Two-dimensional van der Waals materials, Phys. Today **69**, 38 (2016).
[19] S. M. Sze, Y. Li, and K. K. Ng, *Physics of semiconductor devices* (John wiley & sons, 2021).
[20] J. Kang, W. Liu, D. Sarkar, D. Jena, and K. Banerjee, Computational Study of Metal Contacts to Monolayer Transition-Metal Dichalcogenide Semiconductors, Phys. Rev. X **4**, 1 (2014).
[21] A. Allain, J. Kang, K. Banerjee, and A. Kis, Electrical contacts to two-dimensional semiconductors, Nat. Mater. **14**, 1195 (2015).
[22] W. Liu, J. Kang, D. Sarkar, Y. Khatami, D. Jena, and K. Banerjee, Role of metal contacts in designing high-performance monolayer n-type $WSe_2$ field effect transistors, Nano Lett. **13**, 1983 (2013).
[23] D. S. Schulman, A. J. Arnold, and S. Das, Contact engineering for 2D materials and devices, Chem. Soc. Rev. **47**, 3037 (2018).
[24] J. Kang, W. Liu, and K. Banerjee, High-performance $MoS_2$ transistors with low-resistance molybdenum contacts, Appl. Phys. Lett. **104**, 2 (2014).
[25] M. Gurram, S. Omar, and B. J. V. Wees, Bias induced up to 100% spin-injection and detection polarizations in ferromagnet/bilayer-hBN/graphene/hBN heterostructures, Nat. Commun. **8**, 1 (2017).
[26] A. Pal, K. Parto, K. Agashiwala, W. Cao, and K. Banerjee, in IEDM Tech. Dig., Dec. 2019 (2019), pp. 24.2.1–24.2.4.
[27] 2020 IEEE International Roadmap For Devices and Systems (IRDS). Available: https://irds.ieee.org/.
[28] Y. Taur and T. H. Ning, *Fundamentals of Modern VLSI Devices* (Cambridge University Press, Cambridge, 2009).
[29] P. Luo, *et al.*, Doping engineering and functionalization of two-dimensional metal chalcogenides, Nanoscale Horiz. **4**, 26 (2019).
[30] Y. Khatami, H. Li, C. Xu, and K. Banerjee, Metal-to-multilayer-graphene contact part I: Contact resistance modeling, IEEE Trans. Electron Devices **59**, 2444 (2012).
[31] Y. Wang, *et al.*, Van der waals contacts between three-dimensional metals and two-dimensional semiconductors, Nature **568**, 70 (2019).
[32] J. Kang, *et al.*, in IEDM Tech. Dig. (2012), pp. 407–410.
[33] J. Kang, D. Sarkar, Y. Khatami, and K. Banerjee, Proposal for all-graphene monolithic logic circuits, Appl. Phys. Lett. **103**, 1 (2013).
[34] W. Cao, M. Huang, C. H. Yeh, K. Parto, and K. Banerjee, Impact of transport anisotropy on the performance of van der Waals materials-based electron devices, IEEE Trans. Electron Devices **67**, 1310 (2020).
[35] G. Arutchelvan, *et al.*, From the metal to the channel: A study of carrier injection through the metal/2D $MoS_2$ interface, Nanoscale **9**, 10869 (2017).
[36] Á Szabó, A. Jain, M. Parzefall, L. Novotny, and M. Luisier, Electron transport through metal/$MoS_2$ interfaces: Edge- or area-dependent process?, Nano Lett. **19**, 3641 (2019).
[37] Z. Cheng, *et al.*, Immunity to contact scaling in $MoS_2$ transistors using in situ edge contacts, Nano Lett. **19**, 5077 (2019).
[38] Y. Chai, R. Ionescu, S. Su, R. Lake, M. Ozkan, and C. S. Ozkan, Making one-dimensional electrical contacts to molybdenum disulfide-based heterostructures through plasma etching, Phys. Status Solidi Appl. Mater. Sci. **213**, 1358 (2016).
[39] B. H. Moon, *et al.*, Junction-structure-dependent Schottky barrier inhomogeneity and device ideality of monolayer $MoS_2$ field-effect transistors, ACS Appl. Mater. Interfaces **9**, 11240 (2017).
[40] H. Choi, *et al.*, Edge contact for carrier injection and transport in $MoS_2$ field-effect transistors, ACS Nano **13**, 13169 (2019).
[41] C. H. Chu, H. C. Lin, C. H. Yeh, Z. Y. Liang, M. Y. Chou, and P. W. Chiu, End-bonded metal contacts on $WSe_2$ field-effect transistors, ACS Nano **13**, 8146 (2019).
[42] A. Jain, *et al.*, One-dimensional edge contacts to a monolayer semiconductor, Nano Lett. **19**, 6914 (2019).
[43] Z. Yang, *et al.*, A Fermi-level-pinning-free 1D electrical contact at the intrinsic 2D $MoS_2$–metal junction, Adv. Mater. **31**, 1 (2019).
[44] C. C. Cheng, *et al.*, First demonstration of 40-nm channel length top-gate $WS_2$ pFET using channel area-selective CVD growth directly on $SiO_x$/Si substrate, Dig. Tech. Pap. - Symp. VLSI Technol. **2019**, T244 (2019).
[45] L. Wang, *et al.*, One-dimensional electrical contact to a two-dimensional material, Science **342**, 614 (2013).
[46] C. Mead, W. Spitzer, and F. L. Position, Fermi level position at metal-semiconductor interfaces, Phys. Rev. **134**, A713 (1964).
[47] J. Tersoff, Schottky Barrier Heights and the Continuum of Gap States, Phys. Rev. Lett. **52**, 465 (1984).
[48] See Supplemental Material at http://link.aps.org/supplemental/10.1103/PhysRevApplied.15.064068 for more information regarding the semi-classical and atomistic Schottky-barrier modeling and full simulation details and results.
[49] R. T. Tung, Formation of an electric dipole at metal-semiconductor interfaces, Phys. Rev. B - Condens. Matter Mater. Phys. **64**, 1 (2001).
[50] R. T. Tung, The physics and chemistry of the Schottky barrier height, Appl. Phys. Rev. **1**, 011304 (2014).
[51] Y. Y. Illarionov, *et al.*, Insulators for 2D nanoelectronics: The gap to bridge, Nat. Commun. **11**, 3385 (2020).
[52] D. Liu, Y. Guo, L. Fang, and J. Robertson, Sulfur vacancies in monolayer $MoS_2$ and its electrical contacts, Appl. Phys. Lett. **103**, 183113 (2013).
[53] S. McDonnell, R. Addou, C. Buie, R. M. Wallace, and C. L. Hinkle, Defect-dominated doping and contact resistance in $MoS_2$, ACS Nano **8**, 2880 (2014).
[54] Y. Guo, D. Liu, and J. Robertson, Chalcogen vacancies in monolayer transition metal dichalcogenides and Fermi level pinning at contacts, Appl. Phys. Lett. **106**, 173106 (2015).
[55] R. Addou, L. Colombo, and R. M. Wallace, Surface defects on natural $MoS_2$, ACS Appl. Mater. Interfaces **7**, 11921 (2015).
[56] P. Bampoulis, R. Van Bremen, Q. Yao, B. Poelsema, H. J. W. Zandvliet, and K. Sotthewes, Defect dominated charge transport and Fermi Level Pinning in $MoS_2$/metal contacts, ACS Appl. Mater. Interfaces **9**, 19278 (2017).
[57] R. T. Tung, Recent advances in Schottky barrier concepts, Mater. Sci. Eng. R Reports **35**, 1 (2001).

[58] S. Das, H. Y. Chen, A. V. Penumatcha, and J. Appenzeller, High performance multilayer $MoS_2$ transistors with scandium contacts, Nano Lett. **13**, 100 (2013).

[59] C. Maurel, F. Ajustron, R. Péchou, G. Seine, and R. Coratger, Electrical behavior of the Au/$MoS_2$ interface studied by light emission induced by scanning tunneling microscopy, Surf. Sci. **600**, 442 (2006).

[60] M. Abraham and S. E. Mohney, Annealed Ag contacts to $MoS_2$ field-effect transistors, J. Appl. Phys. **122**, 115306 (2017).

[61] E. Gourmelon, J. C. Bernède, J. Pouzet, and S. Marsillac, Textured $MoS_2$ thin films obtained on tungsten: Electrical properties of the W/$MoS_2$ contact, J. Appl. Phys. **87**, 1182 (2000).

[62] C. Kim, *et al.*, Fermi level pinning at electrical metal contacts of monolayer molybdenum dichalcogenides, ACS Nano **11**, 1588 (2017).

[63] Synopsys QuantumATK. Version O-2019.03. [Online]. Available: https://www.synopsys.com/silicon/quantumatk.htm

[64] S. Smidstrup, *et al.*, QuantumATK: An integrated platform of electronic and atomic-scale modelling tools, J. Phys. Condens. Matter **32**, 015901 (2020).

[65] M. Brandbyge, J. L. Mozos, P. Ordejón, J. Taylor, and K. Stokbro, Density-functional method for nonequilibrium electron transport, Phys. Rev. B - Condens. Matter Mater. Phys. **65**, 1654011 (2002).

[66] D. Stradi, U. Martinez, A. Blom, M. Brandbyge, and K. Stokbro, General atomistic approach for modeling metal-semiconductor interfaces using density functional theory and nonequilibrium Green's function, Phys. Rev. B **93**, 28 (2016).

[67] J. P. Perdew, K. Burke, and M. Ernzerhof, Generalized Gradient Approximation Made Simple, Phys. Rev. Lett. **77**, 3865 (1996).

[68] S. Grimme, J. Antony, S. Ehrlich, and H. Krieg, A consistent and accurate ab initio parametrization of density functional dispersion correction (DFT-D) for the 94 elements H-Pu, J. Chem. Phys. **132**, 154104 (2010).

[69] M. V. Bollinger, J. V. Lauritsen, K. W. Jacobsen, J. K. Nørskov, S. Helveg, and F. Besenbacher, One-Dimensional Metallic Edge States in $MoS_2$, Phys. Rev. Lett. **87**, 3 (2001).

[70] J. V. Lauritsen, *et al.*, Size-dependent structure of $MoS_2$ nanocrystals, Nat. Nanotechnol. **2**, 53 (2007).

[71] T. Markussen and K. Stokbro, in Int. Conf. Simul. Semicond. Process. Devices, SISPAD (2016), pp. 373–376.

[72] V. Heine, Theory of surface states, Phys. Rev. **138**, 1689 (1965).

[73] L. Jelver, D. Stradi, K. Stokbro, and K. W. Jacobsen, Schottky barrier lowering due to interface states in 2D heterophase devices, Nanoscale Adv. **3**, 567 (2021).

[74] F. A. Padovani and R. Stratton, Field and thermionic-field emission in schottky barriers, Solid State Electron. **9**, 695 (1966).

[75] Y. Guo, D. Liu, and J. Robertson, 3D behavior of Schottky barriers of 2D transition-metal dichalcogenides, ACS Appl. Mater. Interfaces **7**, 25709 (2015).

[76] W. Mönch, *Semiconductor Surfaces and Interfaces* (Springer, Berlin, 2001).

[77] C. Gong, L. Colombo, R. M. Wallace, and K. Cho, The unusual mechanism of partial Fermi level pinning at metal-$MoS_2$ interfaces, Nano Lett. **14**, 1714 (2014).

[78] G. Hegde and R. Chris Bowen, Effect of realistic metal electronic structure on the lower limit of contact resistivity of epitaxial metal-semiconductor contacts, Appl. Phys. Lett. **105** (2014).

[79] Q. Chen, *et al.*, Atomically flat zigzag edges in monolayer $MoS_2$ by thermal annealing, Nano Lett. **17**, 5502 (2017).

[80] A. Prakash, H. Ilatikhameneh, P. Wu, and J. Appenzeller, Understanding contact gating in Schottky barrier transistors from 2D channels, Sci. Rep. **7**, 1 (2017).

[81] J. Kang, *et al.*, Graphene and beyond-graphene 2D crystals for next-generation green electronics, Proc. SPIE **9083**, 908305 (2014).

[82] C. Yeh, W. Cao, A. Pal, K. Parto, and K. Banerjee, in IEDM Tech. Dig. (2019), pp. 23.4.1–23.4.4.

[83] X. Ling, *et al.*, Parallel stitching of 2D materials, Adv. Mater. **28**, 2322 (2016).

[84] M. Zhao, *et al.*, Large-scale chemical assembly of atomically thin transistors and circuits, Nat. Nanotechnol. **11**, 954 (2016).

[85] W. Hong, G. W. Shim, S. Y. Yang, D. Y. Jung, and S. Y. Choi, Improved electrical contact properties of $MoS_2$-graphene lateral heterostructure, Adv. Funct. Mater. **29**, 1 (2019).

[86] W. Cao, J. H. Chu, K. Parto, and K. Banerjee, A mode-balanced reconfigurable logic gate built in a van der waals strata, npj 2D Mater. Appl. **5**, 1 (2021).

[87] D. Zhang, C. Yeh, W. Cao, and K. Banerjee, 0.5T0.5R—An ultracompact RRAM cell uniquely enabled by van der waals heterostructures, IEEE Trans. Electron Devices **68**, 2033 (2021).

[88] K. Parto, A. Pal, X. Xie, W. Cao, and K. Banerjee, in IEDM Tech. Dig. (2018), pp. 24.1.1–24.1.4.

[89] Y. Gong, *et al.*, Spatially controlled doping of two-dimensional $SnS_2$ through intercalation for electronics, Nat. Nanotechnol. **13**, 294 (2018).

[90] W. Liu, J. Kang, and Kaustav Banerjee, Charactrization of $FeCl_3$ intercalation doped CVD few-layer graphene, IEEE Electron Device Lett. **37**, 1246 (2016).

[91] J. Jiang, J. Kang, W. Cao, X. Xie, H. Zhang, J. H. Chu, W. Liu, and K. Banerjee, Intercalation doped multilayer-graphene-nanoribbons for next-generation interconnects, Nano Lett. **17**, 1482 (2017).

[92] J. Kang, Y. Matsumoto, X. Li, *et al.*, On-chip intercalated graphene inductors for next-generation radio frequency electronics, Nat Electron **1**, 46 (2018).

[93] R. Kappera, *et al.*, Phase-engineered low-resistance contacts for ultrathin $MoS_2$ transistors, Nat. Mater. **13**, 1128 (2014).

[94] D. Saha and S. Mahapatra, Anisotropic transport in 1T′ monolayer $MoS_2$ and its metal interfaces, Phys. Chem. Chem. Phys. **19**, 10453 (2017).

[95] K. Banerjee, S. C. Lin, A. Keshavarzi, S. Narendra, and V. De, in IEEE International Electron Devices Meeting (2003), pp. 36.7.1–36.7.4.